


Tailorable magnetocrystalline anisotropy at the MnPt₃(001) surface

P. Taivansaikhan¹ and D. Odkhuu^{2*}

¹*Department of Physics, Incheon National University, Incheon 22012, South Korea*
²*Institute of Physics and Technology, Mongolian Academy of Sciences, Ulaanbaatar 13330, Mongolia*

 (Received 7 May 2022; revised 30 August 2022; accepted 7 September 2022; published 14 September 2022)

We report results of the density functional theory and density functional perturbation theory calculations on thermodynamic stability, magnetic structure, and magnetocrystalline anisotropy (MCA) of a MnPt₃(001) thin film. It is predicted that the magnetic ground state of the Pt-terminated MnPt₃(001) thin films is the ferromagnetic as found in its bulk structure, while the MnPt termination favors the A-type antiferromagnetic order at the surface. Even more drastic effect of the surface termination on MCA is revealed; in contrast to an in-plane magnetization preferred for the MnPt termination, the Pt-terminated MnPt₃(001) thin films exhibit an extremely large perpendicular MCA (PMCA) up to an order of 10 erg/cm² regardless of its film thickness. Moreover, from detailed single-particle energy spectra analyses, this magnetization reversal is mainly determined by an interplay between two in-plane orbital states, d_{xy} and $d_{x^2-y^2}$ states, of the Pt atom with induced magnetism at the surface, as a result of their energy level changes associated with the Mn 3*d* – Pt 5*d* hybridization. This reported thin-film system can act as a prototype for the in-depth study of the importance of the surface termination with large perpendicular magnetocrystalline anisotropy in spintronic applications.

DOI: [10.1103/PhysRevB.106.104413](https://doi.org/10.1103/PhysRevB.106.104413)

I. INTRODUCTION

Magnetocrystalline anisotropy (MCA) is a spin-orbit coupling (SOC) driven phenomenon with preferred magnetization direction. Thin films with large perpendicular MCA (PMCA) have shown promising results for low-power, high-density, and nonvolatile memories [1–3]. In this research field, the most intensively explored magnetic thin films are FeCo(001) and CoFeB(001), which exhibit large PMCA either at the interface with MgO(001) substrate and/or heavy capping metal (HM) layers including Ta and Pt [4–7]. It is believed that the orbital hybridizations between the 3*d* and 2*p* electronic states at the CoFeB/MgO interface and the 5*d* – 3*d* states at the HM/CoFeB interface are the main origin for large PMCA [4–7]. For the latter interface, the crucial role of HM layers on PMCA has been addressed recently, where the 5*d* orbitals exhibit larger SOC than the 3*d* orbital states [8–10]. Owing to these prerequisites, alloys including 5*d* orbitals, such as Fe – Pt, Co – Pt, and Mn – Pt, have been regarded as potential candidate materials for spintronics applications [11–18].

A large magneto-optic Kerr rotation observed in MnPt₃ alloy has been revisited recently [19–21] as this phenomenon is highly relevant for memory recording devices. Subsequent theoretical works have been performed to elucidate the origin of the large Kerr effects [12,14]. Bulk MnPt₃ has a ferromagnetic (FM) ground state with a high Curie temperature of 460 K [11,22]. However, the main drawback of this magnet is a negligible MCA energy (E_{MCA}) associated with the high-symmetry cubic structure of Cu₃Au phase. Interestingly, it is predicted that MnPt₃(110) thin films have an

antiferromagnetic (AFM) ground state [23]. In addition to these intriguing phenomena on the surface dependent magnetic order, the renewal of research targets seemingly resides in the possibility of large PMCA in a thin-film structure of MnPt₃ and its dependence on the surface and interface terminations, which remain unexplored.

In this paper, using the electronic structure density functional theory (DFT) and density functional perturbation theory (DFPT) calculations, we investigate the thermodynamic stability, magnetic structure, and MCA of bulk MnPt₃ and MnPt₃(001) thin films. Being in consistent with the experimental and previous theoretical studies, MnPt₃ exhibits the FM ground state and acceptable thermal stability in its bulk structure. It is further predicted that the magnetic order and MCA of MnPt₃(001) thin films strongly depend on its surface termination. While the magnetic ground state of the Pt-terminated MnPt₃(001) is FM phase as found in bulk structure, the MnPt termination favors the A-type AFM order at the surface. Moreover, in contrast to an in-plane magnetization of the MnPt-terminated MnPt₃(001), the Pt-terminated films exhibit an extremely large PMCA up to an order of 10 erg/cm² regardless of its film thickness. The underlying mechanism is an interplay between the large spin-orbit coupled in-plane d_{xy} and $d_{x^2-y^2}$ orbital characters of the Pt atom, which has an induced magnetism due to the Mn 3*d* – Pt 5*d* hybridization.

II. COMPUTATIONAL METHODS

The DFT and DFPT calculations were performed using Vienna *ab initio* Simulation Package (VASP) [24] version 5.4.4 within the projector augmented wave (PAW) scheme [25]. Generalized gradient approximation (GGA) by Perdew, Burke, and Ernzerhof (PBE) formulation was used for the

*odkhuu@inu.ac.kr

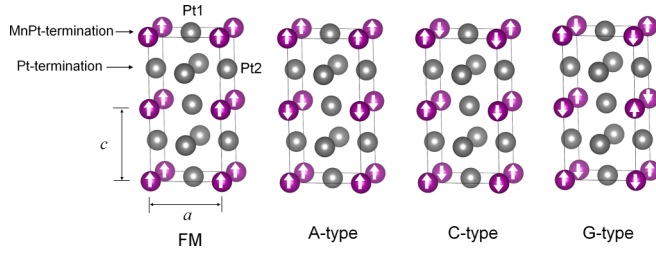


FIG. 1. Atomic and magnetic structures of the FM, A-type, C-type, and G-type AFM phases of MnPt_3 alloy. Purple and gray spheres are Mn and Pt atoms, respectively. Upward and downward arrows superimposed over the sphere represent the spin-up and spin-down magnetic states, respectively.

exchange-correlation potential [26]. As illustrated in Fig. 1, we have considered four different magnetic structures, namely FM, A-type, C-type, and G-type AFM, with a $1 \times 1 \times 2$ supercell of $L1_2$ -type MnPt_3 structure. The A-type, C-type, and G-type AFM phases are regarded as the FM couplings of Mn atoms on the (001), (011), and (111) planes, respectively. In the MnPt_3 structure, there are two distinguishable Pt sites, which we denoted as Pt1 in the MnPt layer and Pt2 in the Pt-only layer on the [001] plane, as indicated in Fig. 1. To investigate the thickness and surface termination dependent magnetic properties of $\text{MnPt}_3(001)$ thin films, two distinct surface terminations, namely Pt termination and MnPt termination, with the thickness range of 1–6 unit cell (u.c; 1 u.c composed of 1 Mn and 3 Pt atoms) layers have been taken into account. In thin-film calculations, we allowed the lattice parameter relaxation along the [001] direction while fixing the lateral lattice parameters on the [001] plane with the optimized lattice constant (3.93 Å) of the bulk FM-phase MnPt_3 . In order to avoid spurious interactions between repeated cells, a vacuum spacing no less than 15 Å perpendicular to the film plane was adopted. We used an energy cutoff of 500 eV and a Monkhorst-Pack k mesh of $9 \times 9 \times 5$ ($9 \times 9 \times 1$) in the Brillouin zone (BZ) for the optimization of bulk (thin film) structure, where all atoms are fully relaxed within the force criteria of 10^{-2} eV/Å. The magnetocrystalline anisotropy energy is determined from total energy differences between two magnetization directions along the [100] and [001]: $E_{\text{MCA}} = E^{[100]} - E^{[001]}$. To ensure convergence of E_{MCA} values, different k -point meshes no less than $21 \times 21 \times 1$ were sampled in noncollinear calculations for the different thicknesses of $\text{MnPt}_3(001)$ films. In the film structure, $E_{\text{MCA}} > 0$ indicates PMCA and $E_{\text{MCA}} < 0$ indicates preference of an in-plane magnetization. The phonon dispersion and thermodynamic properties were carried out by using the PHONOPY code [27] within the harmonic approximation in the DFPT [28]. For the phonon calculations, we employed a $2 \times 2 \times 2$ supercell and a $5 \times 5 \times 5$ k -point mesh in the interpolation of the force constants matrices.

III. RESULTS AND DISCUSSION

Table I summarizes the optimized lattice parameters a and c/a , and relative energies ΔE of the A-type, C-type, and G-type AFM phases with respect to the FM phase for bulk MnPt_3 . The obtained ΔE values are 0.14, 0.11, and

TABLE I. Optimized lattice parameters a (Å) and c/a , relative energies ΔE (eV/u.c) of the A-type, C-type, and G-type AFM phases with respect to the FM phase, and atomic magnetic moment μ_X (μ_B) of MnPt_3 alloy for different magnetic structures.

	a	c/a	ΔE	μ_{Mn}	μ_{Pt1}	μ_{Pt2}
FM	3.93	0.998	0.00	3.78	0.151	0.151
A-type AFM	3.92	0.989	0.14	± 3.77	0.036	0.000
C-type AFM	3.93	0.998	0.11	± 3.77	0.023	0.000
G-type AFM	3.94	1.000	0.78	± 3.78	0.038	0.038

0.78 eV/u.c for the A-type, C-type, and G-type AFM, respectively. These results indicate that the magnetic ground state of bulk MnPt_3 is the FM, as reported by the experimental [11] and previous theoretical studies [18,29]. Hereafter, we thus refer to results of the FM phase in all our discussions for bulk MnPt_3 , unless specified otherwise. Optimized lattice constant of the FM phase is 3.93 Å, which is in reasonable agreement with the experimental (3.90–3.91 Å) [11,30–32] and previous theoretical results (3.93 Å) [29,33]. The Hubbard-type on-site Coulomb energy on Mn $3d$ orbitals is also considered, where the lattice constant increases linearly with the effective U parameter in the DFT + U method and reaches 3.98 Å at $U = 6$ eV.

The absolute values of the spin magnetic moments of Mn and Pt atoms from the standard DFT calculations are shown in Table I. The Mn moment (3.77–3.78 μ_B) does not differ much for the different magnetic structures, while the Pt moment is notably larger in FM (0.151 μ_B) than in AFM phases (0–0.038 μ_B). For the ground-state FM phase, the magnetic moments of the Pt1 and Pt2 atoms are nearly identical as $c/a \approx 1$. Similar findings have been reported in previous calculations; 3.71–3.82 μ_B for Mn and 0.12–0.15 μ_B for Pt [14,29]. A larger magnetic moment of 0.26 ± 0.03 μ_B of the Pt atom has been achieved in an experiment [34,35] although the measured Mn moment of 3.64 ± 0.08 μ_B is almost reproduced in our calculations. This discrepancy is attributable to non-negligible orbital magnetic moment of the Pt $5d$ orbital shells in the experiment [34,35], which is not included in the present magnetic moment shown in Table I. Note that the DFT + U method results in Mn and Pt moments more deviated from the experimental values; thus the results hereafter are referred to those from the standard DFT calculations.

Figures 2(a) and 2(b) present the electronic projected density of states (PDOS) of the Mn and Pt d -orbital states, respectively. Here, we only show the PDOS of the Pt1 atom since the two Pt sites, Pt1 and Pt2, exhibit quite similar features in PDOS. The Mn five d orbitals are degenerate into the t_{2g} and e_g states because of the cubic symmetry crystal field. The strong $d-d$ orbital hybridization between Mn and Pt atoms is apparent: Mn and Pt PDOS have common peaks at the same energy level, especially for the occupied majority-spin and unoccupied minority-spin states near the Fermi level. As a result, the majority-spin PDOS of Mn is almost fully occupied, while the minority-spin states are mainly localized at around 2 eV in the unoccupied band region. Hence, the Mn atom has a large exchange splitting between the spin subbands of the majority-spin and minority-spin states, leading to the

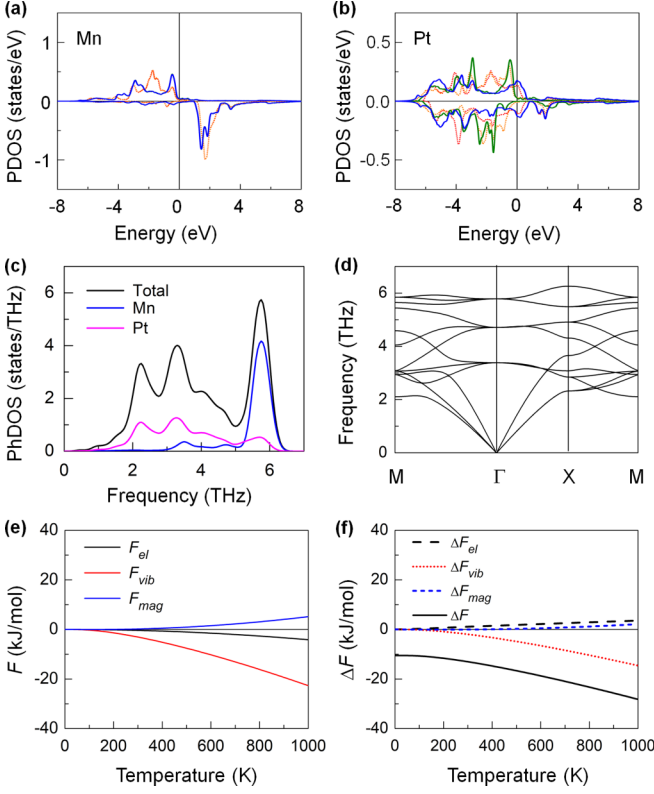


FIG. 2. Electronic projected density of states (PDOS) of the (a) Mn and (b) Pt d -orbital states, (c) phonon density of states (PhDOS), (d) phonon dispersion curve, (e) free energy contributions of the electronic $F_{el}(T, V)$, vibrational $F_{vib}(T, V)$, and magnon $F_{mag}(T, V)$, and (f) free energy change $\Delta F(T, V)$ as function of temperature of the FM-type MnPt_3 alloy. In (a) and (b) the dotted-red, dotted-orange, solid-green, and solid-blue lines represent the d_{xy} , $d_{x^2-y^2}$, d_{yz} , and d_{z^2} orbital characters, respectively. The Fermi level is set to zero energy. In (f) contributions of the electronic $\Delta F_{el}(T, V)$, vibrational $\Delta F_{vib}(T, V)$, and magnon $\Delta F_{mag}(T, V)$ to $\Delta F(T, V)$ are also presented.

significant magnetic moment shown in Table I. In addition, for Pt atom, the strong hybridization between Mn and Pt causes the spin splitting, which in turn leads to the induced magnetism at the Pt site.

From an application perspective, the atomic structure of MnPt_3 alloy must be thermally stable. The Helmholtz free energy can be written as $F(T, V) = E_0(V) + F_{el}(T, V) + F_{vib}(T, V) + F_{mag}(T, V)$, where $E_0(V)$ is the zero-temperature total energy of the system, and $F_{el}(T, V)$, $F_{vib}(T, V)$, and $F_{mag}(T, V)$ are the electronic, vibrational, and magnon contributions of the free energy, respectively. The phase stability against phase decomposition into the most competitive decomposable compounds can be described thermodynamically by the change in the free energy [36,37], $\Delta F = F(\text{MnPt}_3) - F(\text{MnPt}) - 2 \times F(\text{Pt})$, where $F(\text{MnPt}_3)$, $F(\text{MnPt})$, and $F(\text{Pt})$ are the free energies of MnPt_3 , MnPt , and Pt in bulk, respectively.

In order to obtain the thermodynamic properties, we calculated and plotted the phonon DOS (PhDOS) and the phonon dispersion curve of bulk MnPt_3 alloy in Figs. 2(c) and 2(d), respectively. The low-frequency vibrational modes

are predominantly contributed by the Pt atom while the higher frequency modes are those of the Mn, which are associated with the relative atomic weight. Furthermore, no imaginary frequency modes are observed in the phonon dispersion curve shown in Fig. 2(d), which indicates that the structure is stable. From this, the obtained free energy contributions of $F_{el}(T, V)$, $F_{vib}(T, V)$, and $F_{mag}(T, V)$ against temperature are shown in Fig. 2(e). The calculated $F_{el}(T, V)$ and $F_{vib}(T, V)$ decrease as temperature increases, whereas $F_{mag}(T, V)$ increases with temperature. Obviously, the former two contributions, particularly the vibrational, mainly determine the temperature-induced changes in the free energy. The temperature-dependent free energy change $\Delta F(T, V)$ and its contributions, i.e., $\Delta F_{el}(T, V)$, $\Delta F_{vib}(T, V)$, and $\Delta F_{mag}(T, V)$, are shown in Fig. 2(f). The obtained $\Delta F(T, V)$ at 0 K, which corresponds to the formation enthalpy (ΔH_f), is $-10.5 \text{ kJ mol}^{-2}$. This negative value in ΔH_f indicates that MnPt_3 phase is stable at 0 K against its decomposable phases, MnPt and bulk-Pt. As shown in Fig. 2(f), $\Delta F(T, V)$ decreases further as temperature increases, which is almost entirely accounted for by the vibrational contribution. The other two contributions, $\Delta F_{el}(T, V)$ and $\Delta F_{mag}(T, V)$, are insignificant. These results suggest an acceptable thermodynamic stability of MnPt_3 alloy under realistic conditions.

We show the d -orbital resolved E_{MCA} in Figs. 3(a), 3(c) and 3(e) and electronic band structures in Figs. 3(b), 3(d) and 3(f) for the Mn, Pt1, and Pt2 atoms in MnPt_3 , respectively. We find that E_{MCA} of bulk MnPt_3 is approximately -0.1 meV per u.c, which comes predominately from the Pt1 atom (-1.65 meV/atom). On the contrary, the Pt2 (0.78 meV/atom) and Mn (0.003 meV/atom) provide positive contributions to E_{MCA} . Here, the second-order perturbation theory interpretation is adopted [38],

$$E_{\text{MCA}}^{\downarrow\downarrow(\uparrow\uparrow)} = \xi^2 \sum_{o^{\downarrow(\uparrow)}, u^{\downarrow(\uparrow)}} \left[\frac{|\langle \Psi_{o^{\downarrow(\uparrow)}} | L_x | \Psi_{u^{\downarrow(\uparrow)}} \rangle|^2}{E_{u^{\downarrow(\uparrow)}} - E_{o^{\downarrow(\uparrow)}}} - \frac{|\langle \Psi_{o^{\downarrow(\uparrow)}} | L_z | \Psi_{u^{\downarrow(\uparrow)}} \rangle|^2}{E_{u^{\downarrow(\uparrow)}} - E_{o^{\downarrow(\uparrow)}}} \right], \quad (1)$$

$$E_{\text{MCA}}^{\uparrow\downarrow(\downarrow\uparrow)} = \xi^2 \sum_{o^{\downarrow(\uparrow)}, u^{\downarrow(\uparrow)}} \left[\frac{|\langle \Psi_{o^{\downarrow(\uparrow)}} | L_x | \Psi_{u^{\downarrow(\uparrow)}} \rangle|^2}{E_{u^{\downarrow(\uparrow)}} - E_{o^{\downarrow(\uparrow)}}} - \frac{|\langle \Psi_{o^{\downarrow(\uparrow)}} | L_z | \Psi_{u^{\downarrow(\uparrow)}} \rangle|^2}{E_{u^{\downarrow(\uparrow)}} - E_{o^{\downarrow(\uparrow)}}} \right], \quad (2)$$

where Ψ_o (Ψ_u) and E_o (E_u) represent the eigenstate and eigenvalue of an occupied (unoccupied) state, respectively. In Eq. (1), the positive and negative contributions to E_{MCA} are characterized by L_z and L_x matrices of the same spin channel (spin up and up, $\uparrow\uparrow$; spin down and down, $\downarrow\downarrow$), respectively. For the spin-flip channels ($\uparrow\downarrow$, $\downarrow\uparrow$), the L_z and L_x matrices have opposite signs to those of the same spin channels, as formulated in Eq. (2). For the Pt1, the negative E_{MCA} arises primarily from the $\langle xy(\uparrow) | L_x | x^2 - y^2(\downarrow) \rangle$ and $\langle xz/yz(\downarrow) | L_x | z^2(\uparrow) \rangle$ matrix elements, as shown in Fig. 3(c). The mechanism can be associated with the SOC states across the Fermi level at the Γ point [Fig. 3(d)]. The contributions from the other d -orbital pairs are insignificant. On the contrary, these negative contributions have reversed sign for the Pt2 [Fig. 3(e)], where the unoccupied d_{xy} state right at

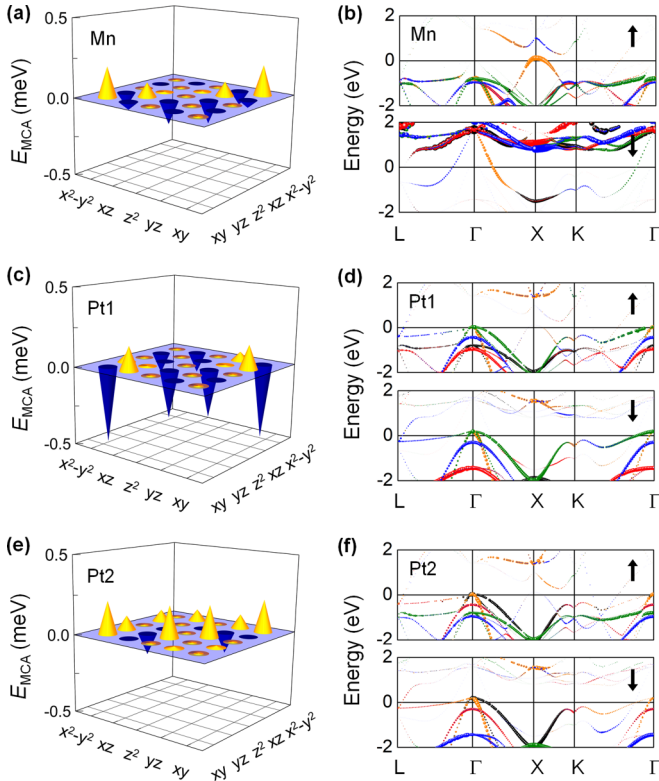


FIG. 3. The d -orbital resolved E_{MCA} and electronic band structure for the (a) and (b) Mn, (c) and (d) Pt1, and (e) and (f) Pt2 atom of $MnPt_3$ alloy. In (a), (c), and (e), yellow and blue cones represent the positive and negative E_{MCA} values, respectively. In (b), (d), and (f), black, orange, green, red, and blue symbols denote the d_{xy} , d_{xz} , d_{yz} , d_{z^2} , and $d_{x^2-y^2}$ orbital characters, respectively. Upward and downward arrows indicate the spin-up and spin-down states, respectively. The size of the symbols represents the weight of d -orbital states. The Fermi level is set to zero energy.

the Γ couples with the occupied $d_{x^2-y^2}$ state. By analyzing in Figs. 3(a) and 3(b), the same argument also applies to Mn as the negative contribution by the $\langle xy(\uparrow)|L_z|x^2 - y^2(\downarrow)\rangle$ changes into positive by the $\langle xy(\downarrow)|L_z|x^2 - y^2(\downarrow)\rangle$ matrix element.

To support the above atomic origin on MCA, we further inspect the orbital magnetic anisotropy defined as $\Delta\mu_o = \mu_o^{[001]} - \mu_o^{[100]}$, where $\mu_o^{[001]}$ and $\mu_o^{[100]}$ are the orbital magnetic moments for magnetization along the [001] and [100] direction, respectively. The obtained $\Delta\mu_o$ ($-0.007 \mu_B$) of the Pt1 atom is more prominent beyond those for the Pt2 ($0.003 \mu_B$) and Mn (zero). For the elemental FM single atomic species with large exchange splitting, E_{MCA} is related to the orbital moment anisotropy via the Bruno formalism [39], $E_{MCA} = (\xi/4\mu_B)\Delta\mu_o$, where ξ is the SOC constant. This expression needs to be modified for structures consisting of multiple atomic species with strong hybridization [40]. Nevertheless, as mentioned above, our calculations show that the Pt1 exhibits $\Delta\mu_o < 0$ and $\Delta\mu_o > 0$ for the Pt2, which adequately obeys the Bruno relation.

We next explore the surface effects on the magnetic structure and E_{MCA} of $MnPt_3(001)$ thin films for the Pt termination and MnPt termination. The model atomic structures of the

TABLE II. Relative energy ΔE (eV/cell), surface energy E_{surf} (eV/ \AA^2), interlayer distance d (\AA) between the surface and subsurface layers, and spin magnetic moments μ_X (μ_B) of Mn and Pt atoms at the surface of $MnPt_3(001)$ thin films for the Pt termination and MnPt termination.

	ΔE	E_{surf}	d	μ_{Mn}	μ_{Pt}
Pt termination					
FM	0.00	-0.588	1.91	3.80	0.16
A-AFM/FM	0.76		1.91	3.78	0.12
C-AFM/FM	0.21		1.91	3.79	0.04
MnPt termination					
FM	0.00		1.94	4.04	0.16
A-AFM/FM	-0.13	-0.591	1.95	4.08	0.10
C-AFM/FM	-0.08		1.95	4.07	0.07

Pt-termination and MnPt-termination layers adopted in the present study are indicated in Fig. 1. For each termination, we have considered three distinct magnetic orders within the surface layer: (1) entirely FM, (2) reconstructed FM with the A-type AFM in the surface layer (i.e., Mn moments in the outermost surface layer couple antiparallel with those in the inner layers), denoted as A-AFM/FM, and (3) reconstructed FM with the C-type AFM in the surface layer (C-AFM/FM). Here, the G-type AFM phase is excluded because of the relatively high energy compared with the other magnetic configurations (Table I). For both terminations, we have also considered the A-AFM and C-AFM orders up to the subsurface layer, which are energetically less stable than the A-AFM/FM and C-AFM/FM configurations.

The calculated relative energies ΔE of the A-AFM/FM and C-AFM/FM to the FM phase, surface energies E_{surf} , and interlayer distance d between the surface (S) and subsurface (S - 1) layers are shown in Table II for the Pt-terminated and MnPt-terminated $MnPt_3(001)$ films with selected thickness of 6 u.c layers. The surface energy is calculated from $E_{surf} = [E(\text{slab}) - \sum_i N_i \mu_i]/2A$, where $E(\text{slab})$ is the total energy of the slab supercell, and N_i and μ_i are the number of atoms and the chemical potential of the i th atomic species. A is the surface area. The chemical potential μ_i can be estimated as the total energy of the elemental ground state structure. As shown in Table II, our total energy calculations indicate that the FM phase is still preserved for the Pt-terminated $MnPt_3(001)$, whereas the MnPt termination favors the A-type AFM phase in the surface layer by ΔE of 0.13 eV/cell. For the most stable magnetic phases, the calculated E_{surf} values are -0.588 and -0.591 eV/ \AA^2 for the Pt termination and MnPt termination, respectively. Such small energy difference between two surface terminations implies that both the Pt termination and MnPt termination may be possible in a real sample. Moreover, with remarkable advances in current fabrication techniques, the different boundary termination layers are now accessible in the surface and interface region upon sample preparation and experimental circumstances. The optimized d values are approximately 1.91 and 1.95 \AA for the Pt termination and MnPt termination, respectively, regardless of the magnetic configurations. As discussed in Table I, the interlayer distance in bulk $MnPt_3$ is 1.97 \AA . Thus, for both terminations, the surface layer displaces toward the subsurface layer due to

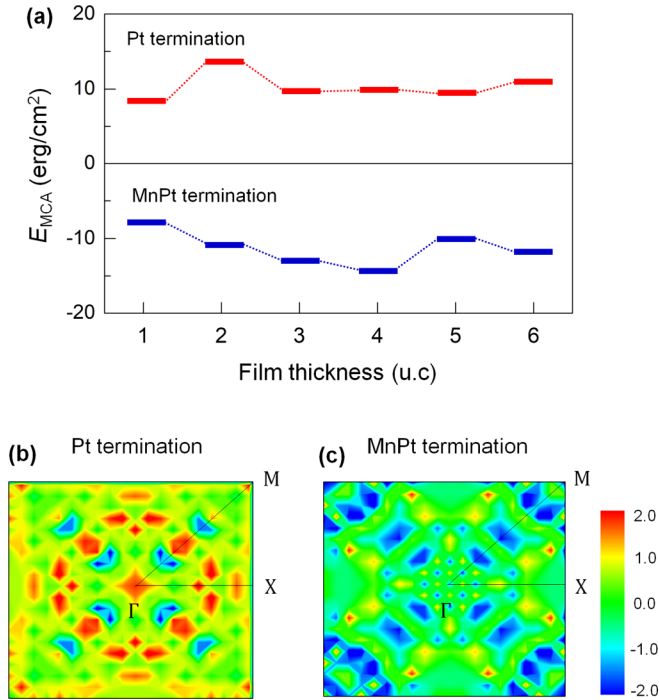


FIG. 4. (a) Thickness dependent E_{MCA} of MnPt₃(001) thin films for the Pt termination (red) and MnPt termination (blue). E_{MCA} distribution over k space, MAE(\mathbf{k}), in the two-dimensional Brillouin zone for the (b) Pt termination and (c) MnPt termination. The energy scale is in unit of meV.

the surface effects (i.e., reduced coordination). Table II also presents the spin magnetic moments of Mn and Pt atoms in the surface layer. The magnetic moments within the subsurface and center layers tend to preserve those in bulk structure and remain unchanged regardless of the film thickness (thus not shown). On the other hand, the obtained magnetic moments of Mn and Pt atoms at the surface are 3.78 – 3.80 and 0.04 – 0.16 μ_B for the Pt termination, respectively, while they are 4.04 – 4.08 and 0.07 – 0.16 μ_B for the MnPt termination.

Figure 4(a) shows the film-thickness dependent E_{MCA} values of MnPt₃(001) thin films for the Pt termination and MnPt termination. For each termination, only the result for the preferred magnetic structure is presented. Obviously, E_{MCA} of MnPt₃(001) can be tuned in sign by the surface termination but not by the film thickness. More specifically, the Pt termination exhibits the strong PMCA, whereas the MnPt termination prefers an in-plane magnetization. For the Pt termination and MnPt termination, the computed E_{MCA} values are 8.6 – 13.7 erg/cm² and –7.7 – (–14.5) erg/cm² for the 1 – 6 u.c. layers, respectively. These PMCA values are up to an order of magnitude larger than the reported experimental values (~ 1.7 erg/cm²) in typical magnetic tunnel junctions, Fe/MgO and CoFeB/MgO [4–8]. The film-thickness independent E_{MCA} indicates that E_{MCA} of MnPt₃(001) is mainly refined in the surface layers. Recall that E_{MCA} for bulk MnPt₃ is very small, in an order of 0.1 meV, as discussed in the previous paragraphs. Hence, in the analysis below we only focus on the film-thickness of 6 u.c. layers for both the Pt termination and MnPt termination.

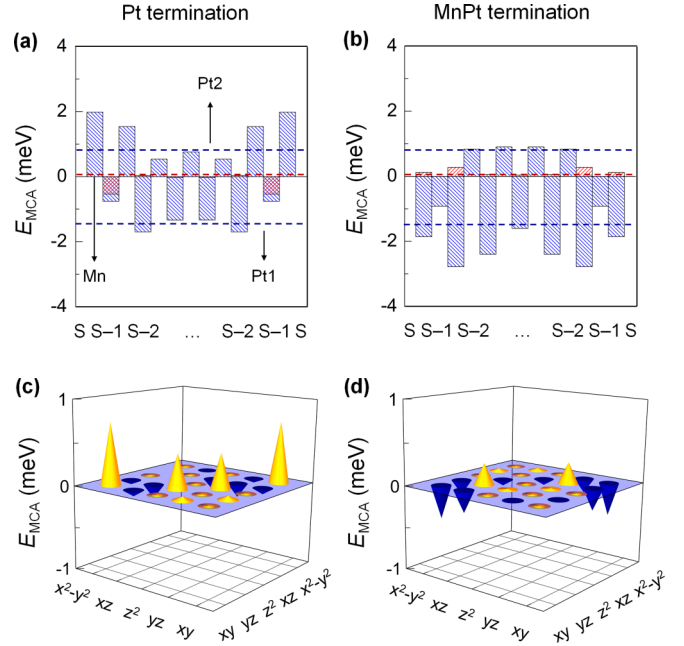


FIG. 5. The layer and atom resolved E_{MCA} of MnPt₃(001) thin films for the (a) Pt termination and (b) MnPt termination. Blue and red bars represent E_{MCA} contributions from Pt and Mn atoms, respectively. Letter S denotes the surface. Dashed blue and red lines represent E_{MCA} values of the Pt1/Pt2 and Mn atoms in bulk MnPt₃, respectively. The d -orbital resolved E_{MCA} of the surface Pt atom for the (c) Pt termination and (d) MnPt termination. Yellow and blue cones represent the positive and negative E_{MCA} values, respectively.

To elucidate the effect of the surface termination on magnetization reversal, we have calculated the k -resolved E_{MCA} according to the force theorem [41,42]

$$E_{MCA}(\mathbf{k}) \approx \sum_{n \in \text{occ}} [\varepsilon(n, \mathbf{k})^{[100]} - \varepsilon(n, \mathbf{k})^{[001]}], \quad (3)$$

where $\varepsilon(n, \mathbf{k})^{[100]}$ and $\varepsilon(n, \mathbf{k})^{[001]}$ are the eigenvalues of the Hamiltonian for magnetization along the [100] and [001] direction, respectively. For all calculations with different thicknesses and terminations, the values of E_{MCA} calculated from the force theorem are in good agreement with those obtained from total energy calculations. In Figs. 4(b) and 4(c) we display counter plots of $E_{MCA}(\mathbf{k})$ in the two-dimensional BZ for the Pt termination and MnPt termination, respectively. Summing over k points, we find E_{MCA} values of 10.9 and –12.1 erg/cm² for the Pt termination and MnPt termination, respectively, which are 10.8 and –11.8 erg/cm² by total energy calculations. For the Pt termination, the main positive contribution to E_{MCA} appears at the Γ point, while it is negative for the MnPt termination. For the MnPt termination, the main negative contributions appear along the Γ M direction and around the M point.

Figures 5(a) and 5(b) present the layer and atom resolved E_{MCA} of MnPt₃(001) thin films for the Pt termination and MnPt termination, respectively. We conclude that E_{MCA} of MnPt₃(001) is mainly determined by the Pt $5d$ orbitals at the surface and subsurface layers: $E_{MCA} > 0$ for the Pt2 atom in the Pt termination and $E_{MCA} < 0$ for the Pt1 in the MnPt termination. The E_{MCA} values decrease as one moves from the

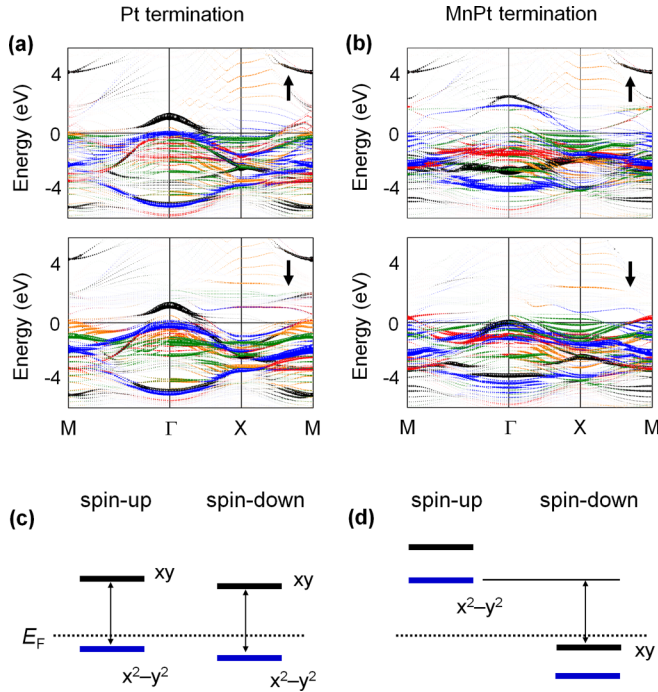


FIG. 6. Majority-spin (upper) and minority-spin (lower panel) electronic band structures of the surface Pt atom of $\text{MnPt}_3(001)$ thin films for the (a) Pt termination and (b) MnPt termination. Black, orange, green, red, and blue symbols denote the d_{xy} , d_{xz} , d_{yz} , d_{z^2} , and $d_{x^2-y^2}$ orbital characters, respectively. The size of the symbols represents the weight of d -orbital states. The Fermi level is set to zero in energy. Simplified schematic diagram for the relative energy level changes of the d_{xy} and $d_{x^2-y^2}$ bands along the ΓM line for the (c) Pt termination and (d) MnPt termination. Horizontal-dashed line indicates the position of the Fermi level (E_F) for reference. The spin-orbit coupling pairs near the Fermi level between the occupied and unoccupied states are emphasized with arrowed vertical lines.

subsurface to the center layers and tend to preserve the bulk-like behavior at the center layers. The overall contribution from the center layers underneath the subsurface layer is thus insignificant. We further decompose E_{MCA} of the surface Pt atom into its $5d$ -orbital resolved components in Figs. 5(c) and 5(d) for the Pt termination and MnPt termination, respectively. Overall, the features of the d -orbital resolved E_{MCA} of the Pt atoms at the surface are almost preserved compared with those in bulk structure [Figs. 3(c) and 3(e)] but significantly larger in the magnitude.

To understand the microscopic origin of MCA at the surface, we plot the electronic band structures of the surface Pt along high-symmetry lines in the two-dimensional BZ in Figs. 6(a) and 6(b) for the Pt termination and MnPt termination, respectively. By analyzing the band characters along with the k -resolved and d -orbital resolved contributions to E_{MCA} , we sketch a simple schematic diagram for the d_{xy} and $d_{x^2-y^2}$ band energy levels along the ΓM line in Figs. 6(c) and 6(d) for the Pt termination and MnPt termination, respectively. Our analysis here largely relies on that for bulk structure discussed in Fig. 3. For the Pt-layer termination, there are significant band pairs between the in-plane d_{xy} and $d_{x^2-y^2}$ states across the Fermi level around the Γ point. Hence, one can argue that the large positive E_{MCA} of the Pt layer at the surface

TABLE III. Interface formation energy H_f ($\text{eV}/\text{\AA}^2$), interlayer distance at the interface $d_{\text{X-O}}$ (\AA), spin magnetic moments μ_{X} (μ_B) of the interfacial Mn and Pt atoms, and E_{MCA} (erg/cm^2) of $\text{MnPt}_3(001)$ thin films on $\text{MgO}(001)$ substrate for different surface (S) and interface (I) terminations.

	H_f	$d_{\text{Mn-O}}$	$d_{\text{Pt-O}}$	μ_{Mn}	μ_{Pt}	E_{MCA}
Pt(S)/Pt(I)	-0.040		2.44	0.12	0.12	8.9
Pt(S)/MnPt(I)	-0.058	2.25	2.30	3.98	0.14	3.2
MnPt(S)/Pt(I)	-0.041		2.45		0.12	-2.3
MnPt(S)/MnP(I)	-0.059	2.25	2.31	3.98	0.14	-7.5

is the result of the SOC pairs between the occupied $d_{x^2-y^2}$ state and the unoccupied d_{xy} state at the Γ and along the ΓM through the $\langle xy|L_z|x^2-y^2\rangle$ matrix element in the perturbation theory [38], in consistent with results of the k -resolved in Fig. 4(b) and d -orbital resolved E_{MCA} in Fig. 5(c). For the MnPt termination in Fig. 6(b), the majority-spin Pt d bands experience overall upward shift compared with those for the Pt termination, where the $d_{x^2-y^2}$ band along the ΓM is located above the Fermi level. However, for the minority-spin, the unoccupied d_{xy} band moves downward across the Fermi level and is occupied. Thus, the positive contributions along the ΓM become diminished; instead, the negative E_{MCA} is mainly predominated by the SOC states, involving the majority-spin $d_{x^2-y^2}$ and minority-spin d_{xy} state across the Fermi level, as indicated in Fig. 6(d).

In a realistic situation, stacking a magnetic memory junction in spintronic devices necessarily involves making contacts with an insulating barrier. One thus needs to take into account the interface effects of $\text{MnPt}_3(001)$ films when in contact with a lattice matching substrate such as $\text{MgO}(001)$. Here, we model the interface supercell composed of 6 u.c. MnPt_3 and five atomic layers of MgO . For the in-plane lattice of $\text{MnPt}_3/\text{MgO}(001)$ supercell, the experimental lattice constant (4.212 \AA) of MgO was adopted. For each surface termination, we have considered two different interface terminations, namely Pt interface [Pt(I)] and MnPt interface [MnP(I)]. Our total energy calculations show that the interfacial Mn and Pt atoms are favored on atop of the O sites in $\text{MgO}(001)$.

Table III presents the calculated interface formation energy H_f , interlayer distances, and spin magnetic moments at the MnPt_3/MgO interface for different surface and interface terminations. The interface formation energy is calculated from $H_f = [E(\text{MnPt}_3/\text{MgO}) - E(\text{MnPt}_3) - E(\text{MgO})]/A$, where $E(\text{MnPt}_3/\text{MgO})$, $E(\text{MnPt}_3)$, and $E(\text{MgO})$ are the total energies of MnPt_3/MgO , MnPt_3 , and MgO , respectively. A is the interface area. All the interface configurations exhibit negative H_f values; about $-0.06 \text{ meV}/\text{\AA}^2$ for the MnPt interface and $-0.04 \text{ meV}/\text{\AA}^2$ for the Pt interface. These results indicate that the MnPt interface is more favorable than the Pt interface. Nevertheless, the latter interface cannot be fully ignored and the formation of the interface layer in a real sample maybe depend on experimental circumstances. As shown in Table III, the interfacial Mn moment is slightly reduced by $0.06 \mu_B$ compared with the surface Mn (Table II) due to the Mn $d - \text{O } p$ hybridization and strain effects, while the Pt moment remains almost unchanged. On the other hand,

the sign of E_{MCA} values of $MnPt_3(001)$ remains the same in the presence of MgO substrate even though its absolute values decrease from 10.8 to 8.9 erg/cm² for the Pt interface and -11.8 to -7.5 erg/cm² for the $MnPt$ interface.

IV. CONCLUSIONS

In summary, using first-principles density functional theory and density functional perturbation theory calculations, we have studied the thermal stability, magnetic structure, and magnetocrystalline anisotropy of bulk $MnPt_3$ and $MnPt_3(001)$ thin films. Although bulk $MnPt_3$ has the FM ground state, the magnetic order of $MnPt_3(001)$ thin films at the surface decisively depends on the surface termination: FM for the Pt termination and A-type AFM coupling for the $MnPt$ termination. We further predict that E_{MCA} is also sensitive

in sign to the surface termination, where the Pt termination favors the strong PMCA whereas in-plane magnetization is preferred for the $MnPt$ -terminated $MnPt_3(001)$. We elucidate the underlying mechanism for the termination-dependent sign change of E_{MCA} by the interplay between the large spin-orbit coupled $5d$ -orbital states of the Pt atom with induced magnetism at the surface. This thin-film system can act as a prototype for the in-depth study of the importance of the surface termination with large perpendicular magnetocrystalline anisotropy in spintronic applications.

ACKNOWLEDGMENT

This work was supported by National Research Foundation of Korea (NRF) Grant No. 2020R1F1A1067589 and Incheon National University Research Grant No. 20190092.

-
- [1] A. V. Khvalkovskiy, D. Apalkov, S. Watts, R. Chepulsii, R. S. Beach, A. Ong, X. Tang, A. Driskill-Smith, W. H. Butler, P. B. Visscher *et al.*, Basic principles of STT-MRAM cell operation in memory arrays, *J. Phys. D: Appl. Phys.* **46**, 074001 (2013).
- [2] C. Chappert, A. Fert, and F. N. V. Dau, The emergence of spin electronics in data storage, *Nat. Mater.* **6**, 813 (2007).
- [3] A. D. Kent and D. C. Worledge, A new spin on magnetic memories, *Nat. Nanotechnol.* **10**, 187 (2015).
- [4] S. Ikeda, K. Miura, H. Yamamoto, K. Mizunuma, H. D. Gan, M. Endo, S. Kanai, J. Hayakawa, F. Matsukura, and H. Ohno, A perpendicular-anisotropy $CoFeB$ - MgO magnetic tunnel junction, *Nat. Mater.* **9**, 721 (2010).
- [5] W. G. Wang, M. Li, S. Hageman, and C. L. Chien, Electric-field-assisted switching in magnetic tunnel junctions, *Nat. Mater.* **11**, 64 (2012).
- [6] C. H. Lambert, A. Rajanikanth, T. Hauet, S. Mangin, E. E. Fullerton, and S. Andrieu, Quantifying perpendicular magnetic anisotropy at the Fe - $MgO(001)$ interface, *Appl. Phys. Lett.* **102**, 122410 (2013).
- [7] K. Nakamura, T. Akiyama, T. Ito, M. Weinert, and A. J. Freeman, Role of an interfacial FeO layer in the electric-field-driven switching of magnetocrystalline anisotropy at the Fe/MgO interface, *Phys. Rev. B* **81**, 220409(R) (2010).
- [8] D. C. Worledge, G. Hu, D. W. Abraham, J. Z. Sun, P. L. Trouilloud, J. Nowak, S. Brown, M. C. Gaidis, E. J. O'Sullivan, and R. P. Robertazzi, Spin torque switching of perpendicular $Ta/CoFeB/MgO$ -based magnetic tunnel junctions, *Appl. Phys. Lett.* **98**, 022501 (2011).
- [9] Y. Shiota, F. Bonell, S. Miwa, N. Mizuochi, T. Shinjo, and Y. Suzuki, Opposite signs of voltage-induced perpendicular magnetic anisotropy change in $CoFeB/MgO$ junctions with different underlayers, *Appl. Phys. Lett.* **103**, 082410 (2013).
- [10] T. Liu, J. W. Cai, and L. Sun, Large enhanced perpendicular magnetic anisotropy in $CoFeB/MgO$ system with the typical Ta buffer replaced by an Hf layer, *AIP Adv.* **2**, 032151 (2012).
- [11] B. Antonini, F. Lucari, F. Menzinger, and A. Paoletti, Magnetization distribution in ferromagnetic $MnPt_3$ by a polarized-neutron investigation, *Phys. Rev.* **187**, 611 (1969).
- [12] P. M. Oppeneer, V. N. Antonov, P. M. Oppeneer, T. Kraft, H. Eschrig, A. N. Yaresko, and A. Y. Perlov, Theory of the giant magneto-optical Kerr effect in $MnPt_3$ and $PtMnSb$, *Solid State Commun.* **94**, 255 (1995).
- [13] K. W. Wierman and R. D. Kirby, Long-range order and magnetic properties of Mn_xPt_{1-x} thin films, *J. Magn. Magn. Mater.* **154**, 12 (1996).
- [14] P. M. Oppeneer, V. N. Antonov, T. Kraft, H. Eschrig, A. N. Yaresko, and A. Y. Perlov, Calculated magneto-optical Kerr spectra of XPt_3 compounds ($X = V, Cr, Mn, Fe$ and Co), *J. Phys.: Condens. Matter* **8**, 5769 (1996).
- [15] T. Kato, H. Ito, K. Sugihara, S. Tsunashima, and S. Iwata, Magnetic anisotropy of MBE grown $MnPt_3$ and $CrPt_3$ ordered alloy films, *J. Magn. Magn. Mater.* **272-276**, 778 (2004).
- [16] D. C. Lee, A. Ghezelbash, C. A. Stowell, and B. A. Korgel, Synthesis and magnetic properties of colloidal $MnPt_3$ nanocrystals, *J. Phys. Chem. B* **110**, 20906 (2006).
- [17] T. Káňa and M. Šob, Mechanical and magnetic properties of Mn - Pt compounds and nanocomposites, *Phys. Rev. B* **85**, 214438 (2012).
- [18] M. P. J. Punkkinen, L. Vitos, K. Kokko, K. Laaksonen, and I. J. Väyrynen, Electronic and magnetic properties of bulk and (100) and (111) surfaces of $MnPt_3$: An *ab initio* study, *Phys. Rev. B* **70**, 024411 (2004).
- [19] P. N. Argyres, Theory of the Faraday and Kerr effects in ferromagnetics, *Phys. Rev.* **97**, 334 (1955).
- [20] T. Kato, H. Kikuzawa, S. Iwata, S. Tsunashima, and S. Uchiyama, Magneto-optical effect in $MnPt_3$ alloy films, *J. Magn. Magn. Mater.* **140-144**, 713 (1995).
- [21] K. W. Wierman, J. N. Hilfiker, R. F. Sabiryanov, S. S. Jaswal, R. D. Kirby, and J. A. Woollam, Optical and magneto-optical constants of $MnPt_3$, *Phys. Rev. B* **55**, 3093 (1997).
- [22] T. H. Kim, M. C. Cadeville, A. Dinia, V. Pierron-Bohnes, and H. Rakoto, Magnetic properties and magnetic phase diagram of the frustrated $Co_{1-x}Fe_xPt_3$, *Phys. Rev. B* **54**, 3408 (1996).
- [23] T. Tohyama, Y. Ohta, and M. Shimizu, Tight-binding calculations of the electronic structure and magnetic properties in ordered TPt_3 ($T = Ti, V, Cr, Mn, Fe$, and Co) alloys, *J. Phys.: Condens. Matter* **1**, 1789 (1989).

- [24] G. Kresse, and J. Furthmüller, Efficient iterative schemes for *ab initio* total-energy calculations using a plane-wave basis set, *Phys. Rev. B* **54**, 11169 (1996).
- [25] P. E. Blöchl, Projector augmented-wave method, *Phys. Rev. B* **50**, 17953 (1994).
- [26] J. P. Perdew, K. Burke, and M. Ernzerhof, Generalized Gradient Approximation Made Simple, *Phys. Rev. Lett.* **77**, 3865 (1996).
- [27] A. Togo and I. Tanaka, First principles phonon calculations in materials science, *Scr. Mater.* **108**, 1 (2015).
- [28] P. Giannozzi, S. de Gironcoli, P. Pavone, and S. Baroni, *Ab initio* calculation of phonon dispersions in semiconductors, *Phys. Rev. B* **43**, 7231 (1991).
- [29] S. C. Hong, Magnetism of the MnPt₃(001) surface: First-principles study, *J. Korean Phys. Soc.* **53**, 1525 (2008).
- [30] K. H. J. Buschow, P. G. Van Engen, and R. Jongebreur, Magneto-optical properties of metallic ferromagnetic materials, *J. Magn. Magn. Mater.* **38**, 1 (1983).
- [31] P. Villars, L. Calvert, *Pearson's Handbook of Crystallographic Data for Intermetallic Phases* (ASM International, Materials Park, OH, 1991).
- [32] R. J. Lange, S. J. Lee, D. W. Lynch, P. C. Canfield, B. N. Harmon, and S. Zollner, Ellipsometric and Kerr-effect studies of Pt₃-X (X = Mn, Co), *Phys. Rev. B* **58**, 351 (1998).
- [33] A. Jezierski, A study of the electronic structure of Pt, Mn alloys by the LMTO method, *J. Phys.: Condens. Matter* **2**, 493 (1990).
- [34] E. T. Kulatov, Y. A. Uspenskii, and S. V. Halilov, Spin, orbital moments and magneto-optical properties of MPt₃ (M = Cr, Mn, Fe, Co) compounds, *J. Magn. Magn. Mater.* **163**, 331 (1996).
- [35] S. J. Pickart and R. Nathans, Alloys of the first transition series with Pd and Pt, *J. Appl. Phys.* **33**, 1336 (1962).
- [36] H. İ. Sözen, S. Ener, F. Maccari, K. P. Skokov, O. Gutfleisch, F. Körmann, J. Neugebauer, and T. Hickel, *Ab initio* phase stabilities of Ce-based hard magnetic materials and comparison with experimental phase diagrams, *Phys. Rev. Materials* **3**, 084407 (2019).
- [37] N. R. Mediukh, V. I. Ivashchenko, D. A. Pogrebnjak, and V. I. Shevchenko, First-principles study of thermodynamic and stability properties of TiC-SiC alloys, in *2016 International Conference on Nanomaterials: Application & Properties (NAP)*, 01NTF4 (2016).
- [38] D. S. Wang, R. Wu, and A. J. Freeman, First-principles theory of surface magnetocrystalline anisotropy and the diatomic-pair model, *Phys. Rev. B* **47**, 14932 (1993).
- [39] P. Bruno, Tight-binding approach to the orbital magnetic moment and magnetocrystalline anisotropy of transition-metal monolayers, *Phys. Rev. B* **39**, 865 (1989).
- [40] C. Andersson, B. Sanyal, O. Eriksson, L. Nordström, O. Karis, D. Arvanitis, T. Konishi, E. Holub-Krappe, and J. Hunter Dunn, Influence of Ligand States on the Relationship between Orbital Moment and Magnetocrystalline Anisotropy, *Phys. Rev. Lett.* **99**, 177207 (2007).
- [41] M. Weinert, R. E. Watson, and J. W. Davenport, Total-energy differences and eigenvalue sums, *Phys. Rev. B* **32**, 2115 (1985).
- [42] G. H. O. Daalderop, P. J. Kelly, and M. F. H. Schuurmans, First-principles calculation of the magnetocrystalline anisotropy energy of iron, cobalt, and nickel, *Phys. Rev. B* **41**, 11919 (1990).